Journal of Solid State Chemistry 308 (2022) 122945

Contents lists available at ScienceDirect

Journal of Solid State Chemistry

journal homepage: www.elsevier.com/locate/jssc

Interconnected effects of direct Gd doping and accompanying indirect Te-stoichiometry destroying on the thermoelectric properties of Te-rich $Bi_{2-x}Gd_xTe_{3+y}$ compounds

Maxim Yaprintsev [a], Oleg Ivanov [b,*], Alexei Vasil'ev [b]

[a] Belgorod State University, Belgorod, 308015, Russia
[b] Belgorod State Technological University Named After V.G. Shukhov, Belgorod, 308012, Russia

ARTICLE INFO

Keywords:
Bismuth telluride
Nonstoichiometric compounds
Point defects
Electronegativity
Energy gap
Thermoelectric properties

ABSTRACT

Solvothermal synthesis and spark plasma sintering were applied to prepare Te-rich $Bi_{2-x}Gd_xTe_{3+y}$ compounds with 1; 2; 3 and 4 at. % Gd. To synthesize the Te-rich compositions, 3 at. % Te excess was introduced into all the starting powders with different *x*. Under sintering, high-temperature Te evaporation occurred. Owing to difference in electronegativity of Bi and Gd, resulting in increasing of ionicity degree and relevant strengthen of polar covalent Bi(Gd)-Te bond, a rate of the Te evaporation is remarkably decreasing with increasing *x*. As result, the *x* (Gd content) and *y* (Te content) coefficients happen to be interconnected. Specific point defects are formed via direct Gd doping (dopant Gd atoms substituting for Bi) and indirect destroying Te-stoichiometry (interstitial Te atoms and anti-site Te_{Bi} defects). Effects of these defects on the thermoelectric properties of the $Bi_{2-x}Gd_xTe_{3+y}$ compounds with interconnected *x* and *y* coefficients were explored in detail. Specific anomalies of all the thermoelectric properties (the specific electrical resistivity, the Seebeck coefficient and the total thermal conductivity), related to onset of intrinsic electrical conductivity, are shifted to higher temperatures with increasing Gd content, which is accompanying by increasing Te content. This *x*(*y*)-dependent shifting can be originated from increasing energy gap, which is, in turn, due to strengthen of polar covalent Bi(Gd)-Te bonds in the Gd-doped samples. The best thermoelectric properties are observed in the composition with 1 at. % Gd and 59.94 at. % Te. This composition is very close to Te-stoichiometric one and is optimal, since it has minimal electron concentration and maximal electron mobility.

1. Introduction

At present, two main strategies are usually applied to enhance thermoelectric efficiency of material [1–3]. First of them is based on developing new thermoelectric materials having a combination of the thermoelectric properties, which is suitable to maximize the thermoelectric figure-of-merit of the material. Currently, many materials including the Hausler alloys [4], silicides [5], selenides [6] and sulfides [7] of some metals, medium-entropy and high-entropy alloys [8,9] and complex oxides [10] have been considered as promising ones. However, these materials are now under intensive and detailed examination to estimate their opportunities to be reliable, repeatable in the properties under thermo-cycling and etc. This examination should be preceding applying the materials in various thermoelectric devices. The second strategy is based on modifying common thermoelectric materials, which are already applied to construct various commercial thermoelectric devices (Bi_2Te_3-based alloys, Pb-Te, SiGe). There are many scientific and technological ways to improve the thermoelectric properties of these materials, which are based on modern approaches of engineering of defects [11–13], including phonon and band engineering, developing various nanostructures and low-dimensional systems [14–16] and etc.

Bismuth telluride, Bi_2Te_3, and Bi_2Te_3-based alloys are known to be the best materials for various thermoelectric applications around room temperature [17]. A number of investigations using various physical and technological approaches have been carried out to enhance thermoelectric efficiency of Bi_2Te_3, and Bi_2Te_3-based alloys. The main approaches are as follows: 1) an optimization of composition and thermoelectric properties by doping with various elements [18–26] or via forming the solid solutions and new chemical compounds, based on starting Bi_2Te_3, or Bi_2Te_3-based alloys [27–29] (in this case both the

* Corresponding author.
E-mail address: Ivanov.Oleg@bsu.edu.ru (O. Ivanov).

https://doi.org/10.1016/j.jssc.2022.122945
Received 29 November 2021; Received in revised form 20 January 2022; Accepted 25 January 2022
Available online 29 January 2022

electrical conductivity via carrier concentration and the thermal conductivity via forming the specific defect structure can be controlled); 2) nanostructuring the material resulting in reducing the thermal conductivity via phonon scattering by interfaces, and increasing the Seebeck coefficient via a change of density of states near the Fermi level in low-dimensional systems [30] or via electron energy filtering phenomenon [31].

Elemental doping of Bi_2Te_3, and Bi_2Te_3-based alloys is one of fruitful and promising routes, which applies to tune all the thermoelectric properties (the specific electrical resistivity, ρ, the Seebeck coefficient, S, and the total thermal conductivity, k) in desired manner, resulting in maximizing the thermoelectric figure-of-merit, ZT, of the compounds. Introducing dopant atoms into crystal Bi_2Te_3 structure usually leads to forming point defects of various natures, which can act as donor or acceptor centres, as well as scattering centres for electron and phonons, form an impurity band with resonance energy levels, etc. Besides forming these intrinsic point defects, which are directly related to doping itself, forming other defects can be also induced via various mechanisms as result of this doping, which should be considered as defects accompanying the doping. The Bi-Te bonds in Bi_2Te_3-based compounds are polar covalent [32,33]. In general, strength of polar covalent bond is dependent on its ionicity degree [34]. In turn, the ionicity degree is governed by difference in electronegativity of the *A* and *B* atoms, which are chemically interacting [35]. Under doping with some element *D*, difference in electronegativities of the interacting atoms for the *D-B* or *A-D* pairs can be remarkably differed as compared to that for the *A-B* pair. Therefore, under *D*-doping, the strength of polar covalent bond in solid, which is constructed from the interacting *A-B* atoms, will be changed. One can conclude that the strength of polar covalent Bi-Te bonds in Bi_2Te_3--based compounds can be changed under elemental doping, too. Under high-temperature treatment, Te is easy evaporating from these compounds that will result in destroying Te-stoichiometry and, hence, forming specific point defects. Efficiency of the Te-evaporation is dependent on the strength of polar covalent Bi-Te bonds. Changing this strength in doped Bi_2Te_3-based compounds can affect the Te-evaporation and, hence, the Te content.

The aim of this paper is to analyze features in the thermoelectric properties of the $Bi_{2-x}Gd_xTe_{3+y}$ compounds. In these compounds, the Gd doping with various x results in relevant changing in the Te content, y, i.e. x and y happen to be interconnected. Therefore, the Gd effect and the Te effect on the thermoelectric properties of $Bi_{2-x}Gd_xTe_{3+y}$ happen to be interconnected effects, too. The Gd effect is due to direct Gd doping, whereas the Te effect is accompanying one, which is induced by changing in Te sublattice due to the Gd doping. It should be noted that Gd is transient *f*-metal, which is ferromagnetically ordering below 292 K [36]. The Kondo effect and various types of magnetic ordering can be often observed in solid with magnetic impurities. Besides, Bi_2Te_3 is topological insulator [37]. Embedding magnetic impurities in topological insulator is effective way to examine features in the topological properties. However, various physical phenomena related to magnetic impurities, are usually observed at low temperatures (below ~50 K). In this paper, the properties of the Te-rich thermoelectric $Bi_{2-x}Gd_xTe_{3+y}$ compounds are studied above room temperature. Therefore, no magnetic effects of the Gd dopants on properties of these compounds will be considered. However, research of low-temperature transport properties of the compounds will be carried out in the future.

2. Materials and methods

The starting $Bi_{2-x}Gd_xTe_{3+y}$ powders with x=0.05; 0.1; 0.15 and 0.2 were prepared by using technology rout based on solvothermal synthesis, which is reported in detail in Ref. [38]. For these x values, the Gd content is equal to 1, 2, 3 and 4 at. %, respectively. For synthesis, $Bi(NO_3)_3{\cdot}5H_2O$ and $Gd(CH_3COO)_3{\cdot}4H_2O$ were taken in stoichiometric ratio in accordance with x, whereas TeO_2 was taken in excess on the basis that the excess tellurium content would be 3 at. % in all the synthesized powders with different x. These components were firstly dissolving in a mixture of 450 cm^3 ethane-1,2-diol NaOH and 15 g NaOH under vigorous stirring by a magnetic stirrer. Then, poly(1-ethenylpyrrolidin-2-one) (M_r=12000) was added to the reaction mixture. After vigorous stirring for 30 min, this mixture was put in autoclave. The auroclave was sealed and maintained at 463 K for 5 min and then cooled naturally to room temperature. After completing the solvothermal synthesis, dark grey precipitate was taken out by centrifuging and washed with deionized water and ethyl alcohol several times and then dried at 353 K for 8 h. To prepare the bulk samples, the starting powders were treated by spark plasma sintering (SPS) at pressure of 40 MPa and temperature of 680 K for 2 min in vacuum. As result, the Ø20 mm × 15 mm cylinders were sintered. To explore the thermoelectric properties of the samples, 2 × 2 × 10 mm bars and Ø10 × 2 mm disks were cut.

Crystal structure and phase composition of the starting powders and the bulk samples were examined by X-ray diffraction (XRD) analysis, performed by using a Rigaku Ultima IV diffractometer with CuK_α-radiation. Correct elemental composition of the bulk samples was extracted by a Shimadzu ICP (Inductively Coupled Plasma) emission spectrometer ICPE-9000. Grain structure features in the bulk samples were observed using scanning electron microscopy (SEM) by using a Nova NanoSEM 450 microscope. To measure density of the bulk samples, the Archimedes method was applied. The specific electrical resistivity, ρ, and the Seebeck coefficient, S, of the bar samples were measured by using a ZEM-3 system. The total thermal conductivity, k, of the disk-shaped samples was measured by a TC-1200 system with using a laser flash method. A Mini Cryogen Free Measurements System (Cryogenic Ltd, UK) was applied to examine the Hall effect and estimate concentration, n, and Hall mobility, μ_H, of majority carriers.

3. Results and discussion

3.1. Characterization of the starting $Bi_{2-x}Gd_xTe_{3+y}$ powders

Resulted from XRD analysis, phase composition of all the starting powders with different x is a combination of major rhombohedral $R\bar{3}m$ phase, typical for pure Bi_2Te_3, and minor trigonal $P321$ phase, corresponding to elemental Te. As an example, XRD pattern for the powder with x=0.2 is shown in Fig. S1. The minor Te phase is forming expectedly, since excess Te was preliminary introduced into all the starting powders. Since difference between ionic radii of Bi^{3+} (1.10 nm) and Gd^{3+} (1.078 nm) is small enough [39], no Gd doping effect on lattice Bi_2Te_3 parameters was observed in XRD patterns, taken for compositions with different x. Using the Rietveld refinement method, lattice parameters, a=b and c, for all the starting powders were calculated as 4.387 and 30.492 Å, respectively. All the starting powders mainly consisted of hexagonal plate-shaped two-dimensional (2D) particles. Average lateral size of the plates and their width were estimated as several hundreds of nm and of ~100 nm, respectively. Forming the plate-shaped 2D-particles is related to specific features in crystal structure and chemical bonding of Bi_2Te_3-based alloys [1,2,17]. Analysis of elemental composition of the $Bi_{1.9}Gd_{0.1}Te_3$ particles was earlier reported in Ref. [38]. It was shown that, firstly, Gd is really inserted in the particles, and, secondly, all the elements (Bi, Gd, Te) are uniformly distributed within the particles. Moreover, paramagnetic resonance absorption spectra of the $Gd_xBi_{2-x}Te_3$ alloys with $0<x<0.2$ were earlier measured at room temperature [40]. These data showed that Gd^{3+} site has the C_{3v} symmetry, indicating a true substitution of Bi atoms by Gd.

3.2. High-temperature Te evaporation from the bulk $Bi_{2-x}Gd_xTe_{3+y}$ samples during SPS-process

Density of the bulk samples after SPS treatment was weakly and irregularly x-dependent. Maximum density value is ~7.64 $g{\cdot}cm^{-3}$ for

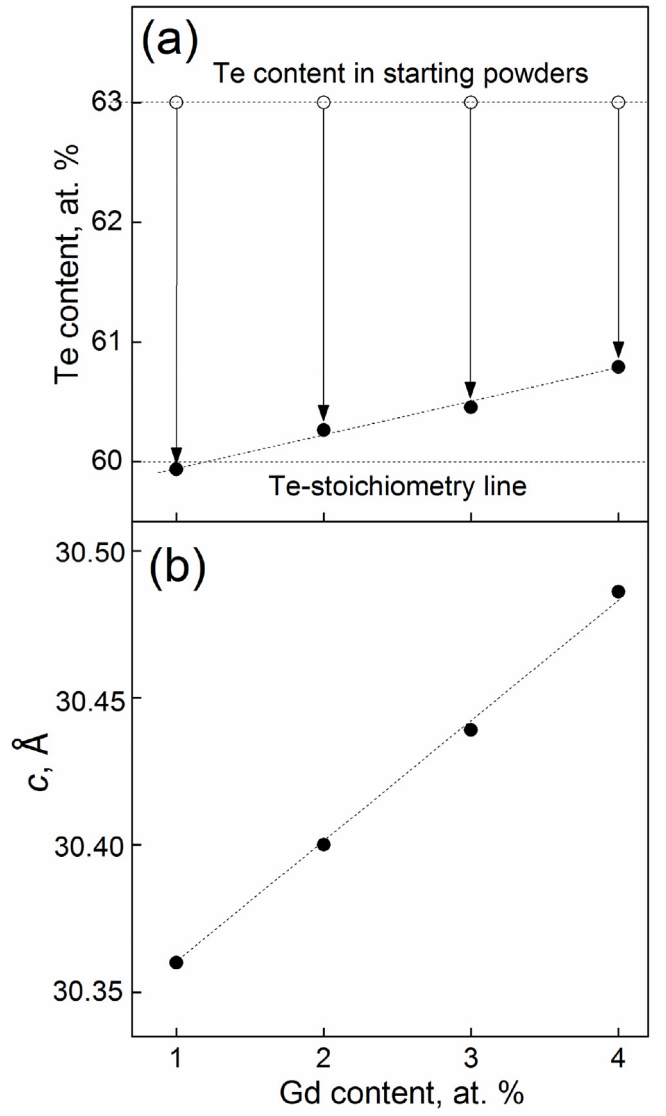

Fig. 1. Effect of the Gd doping on Te content (a) and lattice *c* parameter (b) in the $Bi_{2-x}Gd_xTe_{3+y}$ compounds.

x=0.1 that is ~99.2% of theoretical value of the Bi_2Te_3 density (7.7 g/cm^3), and minimum value is 7.32 g·cm^{-3} for x=0.2 (~95%).

Any high-temperature treatment of Bi_2Te_3-based compounds is unavoidably accompanied by Te evaporation, resulting in changing initial stoichiometry of the compounds. Energy of Te evaporation is known to be much lower than that of Bi (52.55 kJ·mol^{-1} for Te against 104.80 kJ·mol^{-1} for Bi [26]). As result, at high temperatures, Te will be evaporated much easier as compared to Bi. Elemental composition of the bulk $Bi_{2-x}Gd_xTe_{3+y}$ samples, sintered from the relevant starting powders via SPS-process, was also sufficiently changed. This change is due to high-temperature Te evaporation during sintering. The Te content in the sintered $Bi_{2-x}Gd_xTe_{3+y}$ samples, which were prepared from the starting powders with initial Te excess (3 at. %), happened to be x-dependent (Fig. 1 (a)). The Te evaporation process is schematically shown by arrows. With decreasing x, the Te content is linearly falling from maximum value equal to 60.79 at. % (for 4 at. % Gd) down to minimum value equal to 59.94 at. % (for 4 at. % Gd). For the x=0.05; 0.1; 0.15 and 0.2, y is equal to −0.003 and + 0.013; +0.023 and + 0.04, respectively. The minimal Te content is close to the Te content for Te-stoichiometric $Bi_{1.9}Gd_{0.1}Te_3$ composition. Other compositions with different Te content lie above Te-stoichiometry line, i.e. they still remain the Te-rich compositions like the relevant starting powders. Since the x and y coefficients are linearly connected to each other, the x (the Gd content) and y (the Te content) coefficients happen to be inter-dependent.

XRD patterns of all the bulk samples correspond to single phase with space symmetry $R\bar{3}m$ group. No traces of other phases were observed. Lattice *c* parameter is gradually growing with increasing x (Fig. 1 (b)). Lattice *a* parameter is x-independent. The Te-rich $Bi_{2-x}Gd_xTe_{3+y}$ compounds are nonstoichiometric compounds of cation interstitialcy type, in which destroying Te-stoichiometry will result in forming interstitial Te atoms and anti-site defects of Te in Bi-sites (Te_{Bi}), which are key structure elements of nonstoichiometric compounds [41]. Ionic radius of Te^{2-} (2.21 nm) is much bigger than ion radii of Bi^{3+} (1.078 nm) [39]. As result, forming the anti-site Te_{Bi} defects should be accompanied by expansion of unit cell. Besides, the interstitial Te atoms can be also responsible for gradual increasing in lattice *c* parameter with increasing the Te content.

In general, increasing the Te content with increasing the Gd content, which is observed in our experiments, can be related to relevant reducing

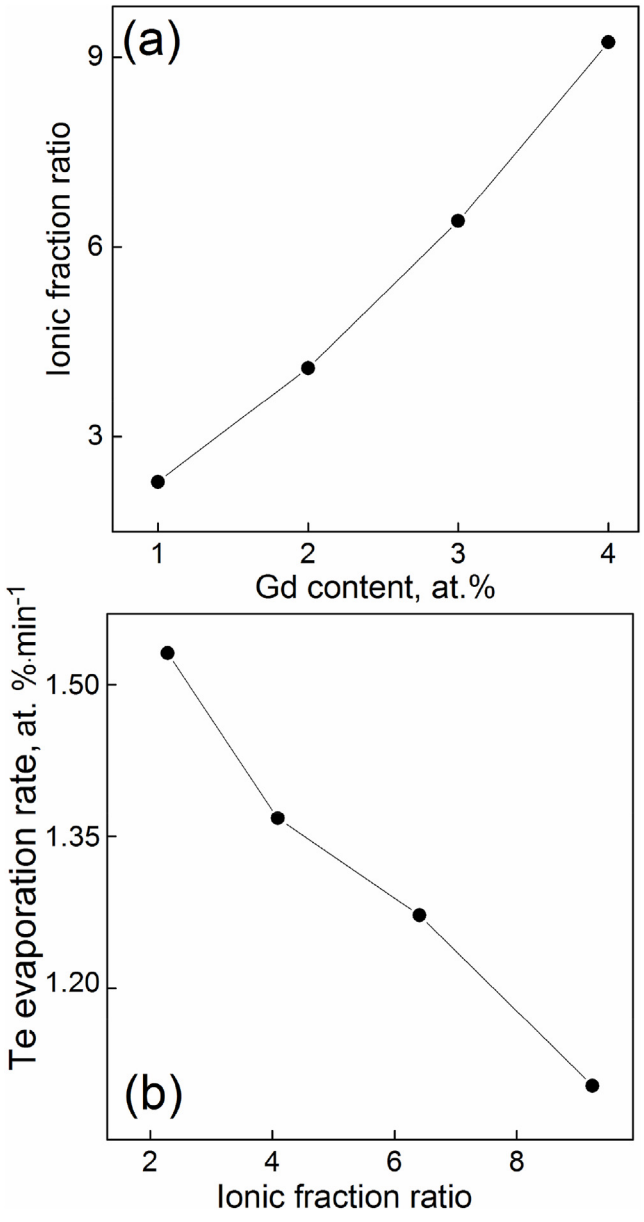

Fig. 2. (a) Dependence of ionic fraction ratio on Gd content; (b) dependence of Te evaporation rate on ionic fraction ratio in the $Bi_{2-x}Gd_xTe_{3+y}$ compounds.

a rate of the Te evaporation. In turn, this reducing can be originated from more strength of chemical Gd-Te bond as compared to that for Bi-Te bond. The strength of a chemical bond depends on its energy, i.e. the greater energy results in the stronger strength. Change of the strength of Bi(Gd)-Te bonds in the $Bi_{2-x}Gd_xTe_{3+y}$ compositions with increasing x can be attributed to difference in electronegativities of Bi and Gd. The crystal Bi_2Te_3 structure is layered one, in which five individual atomic layers are stacked in the following order [1,2,17].

Te(1)–Bi–Te(2)–Bi–Te(1) (1)

where Te(1) and Te(2) denote two types of the Te atoms in the lattice.

Crystal c-axis is perpendicular to the layers, whereas crystal (*a*–*b*)-planes are oriented along the layers. The neighboring layers are bonded via weak Van-der-Waals interaction. The chemical bonding between atoms within the layers is dominantly strong covalent with small fraction of ionic bonding, i.e. this bonding is in fact polar covalent one. Ionic bonding fraction, *I.F.*, can be introduced to characterize an ionicity degree for polar covalent bond. Using the empirical Pauling approach, *I.F.* can be attributed to difference between the electronegativities of the interacting *A* (X_A) and *B* (X_B) atoms (ions) as follows [35].

$$I.F. = 1 - \left[\exp\left\{-\frac{(\Delta X)^2}{4}\right\}\right] \quad (2)$$

where $\Delta X = X_A - X_B$.

For Gd-doped Bi_2Te_3, *I.F.* can be changed, since the electronegativity of the Bi and Gd atoms are different. Actually, by partial substituting of A or/and B ions for other C ion (C-doping), *I.F.* will be increased (at X_A-$X_C > X_A$-X_B or X_C-$X_B > X_A$-X_B that will results in increasing ΔX) or decreased (at X_A-$X_C < X_A$-X_B or X_C-$X_B < X_A$-X_B that will results in decreasing ΔX). The electronegativities of Bi, Te and Gd are X_{Bi}=2.02, X_{Te} =2.10 and X_{Gd}=1.20 [35]. Since X_{Te}-$X_{Gd} > X_{Te}$-X_{Bi}, *I.F.* in $Bi_{2-x}Gd_xTe_{3+y}$ should be gradually increasing with increasing x. Expression (2) was applied to roughly estimate changing in *I.F.* in the $Bi_{2-x}Gd_xTe_{3+y}$ compounds with different x. Difference in the Te(1)-Bi and Te(2)-Bi bonds was neglected. Since only partial substitution of Gd for Bi occurred, the $X_{Bi\text{-}Gd}=[(1\text{-}x)\cdot X_{Bi} + x\cdot X_{Gd}]$ expression was applied to calculate changing in the X_{Bi} and X_{Gd} contributions into the total electronegativity of the $Bi_{2-x}Gd_xTe_{3+y}$ compounds. The calculated *I.F.* values are too small, although relative changing in *I.F.* is large enough. Therefore, *I.F.* was next recalculated to an ionic fraction ratio, $I.F.R.=I.F.(x)/I.F.(x=0)$. That is, changing the electronegativity was considered in relation to the undoped Bi_2Te_3. The *I.F.R.* vs. Gd content dependence is presented in Fig. 2 (a). *I.F.R.* is growing with increasing x. Maximal *I.F.R.* value is equal to ~9.25 for 4 at. % Gd.

In accordance with the Pauling's approach, the energy of polar covalent bond increases with growing the iconicity degree, which is, in turn, dependent on difference between the electronegativites of atoms being chemically bonding [34]. For two atoms, *A* and *B*, with the electronegativites of X_A and X_B, the energy of its bonding can be calculated by the Pauling's method

$$E(A-B) = [E(A-A) + E(B-B)]^{1/2} + 30(\Delta X_{AB})^2 \quad (3)$$

where *E*(*A*-*A*) and *E*(*B*-*B*) are energies of a normal covalent bond between the same atoms and $\Delta X_{AB} = X_A$-X_B.

In accordance with expression (3), gradual Gd doping will result in relevant increasing the ionicity degree in the $Bi_{2-x}Gd_xTe_{3+y}$ compounds (Fig. 2 (a)) and, hence, in relevant increasing the energy of polar covalent bond. Increasing the energy bond will weaken the high-temperature Te evaporation. Fig. 2 (b) shows changing in Te evaporation rate with increasing the ionic fraction ratio. The Te evaporation rate was calculated as changing in Te content during SPS-process (difference between Te content in the bulk sample and in the relevant starting powder) per duration of process itself (2 min). One can see that the strength of polar covalent bond, which is expressing via *I.F.R.*, remarkably affects efficiency of the Te evaporation.

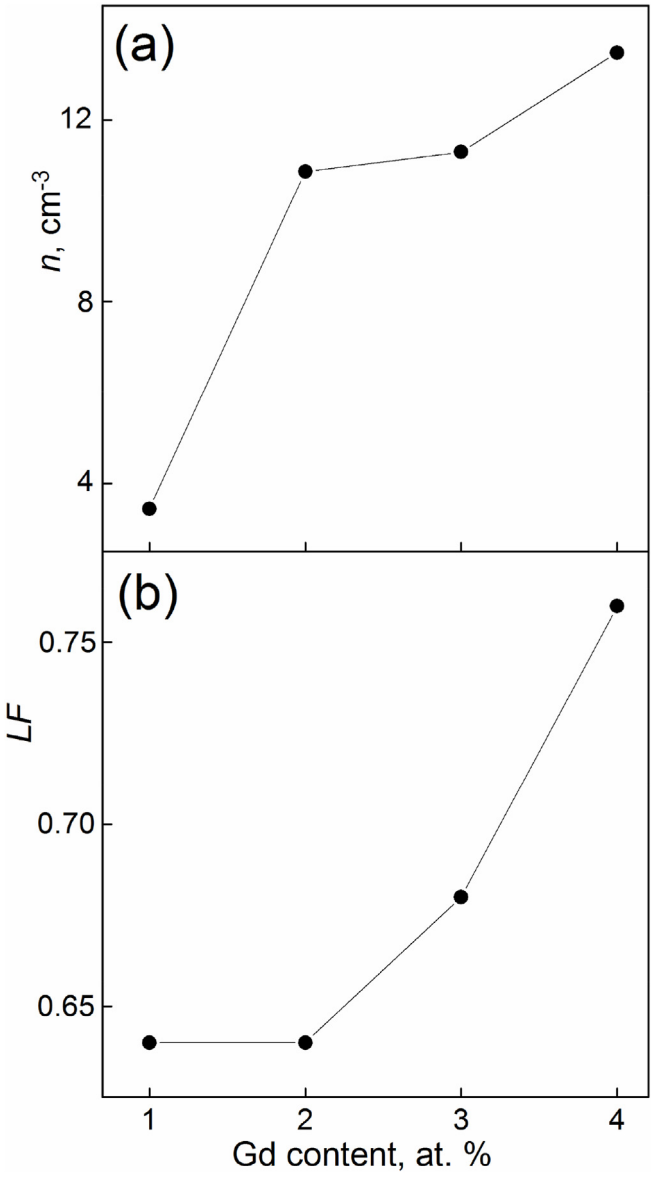

Fig. 3. Effect of Gd doping on electron concentration (a) and the Lotgering factor (b) in the $Bi_{2-x}Gd_xTe_{3+y}$ compounds.

3.3. Features in the thermoelectric properties of the bulk $Bi_{2-x}Gd_xTe_{3+y}$ samples

Key parameter affecting all the thermoelectric properties of material is concentration of majority carriers. For the $Bi_{2-x}Gd_xTe_{3+y}$ compounds with different x, the majority carriers are electrons. The $n(x)$ dependence for these compounds is shown in Fig. 3 (a).

With increasing x, n is steady growing. Minimal n is observed for the composition with 1 at. % Gd. This composition is very close to the Te-stoichiometric one, too. Generally, both type and concentration of the carriers in Bi_2Te_3-based alloys are directly related to various point defects [18–20]. Under the Gd doping, isovalent substitution of Gd^{3+} for Bi^{3+} occurs in the crystal Bi_2Te_3 structure. This substitution cannot directly affect the carriers concentration. However, it is known that various rare earth elements, *R* (*R*=Lu, Tm, Gd, La, Ce, etc.), act as donor centres in crystal Bi_2Te_3 structure [25,26,42–45]. For the nonstoichiometric Te-deficient Bi_2Te_3 compounds, this donor-like effect is usually

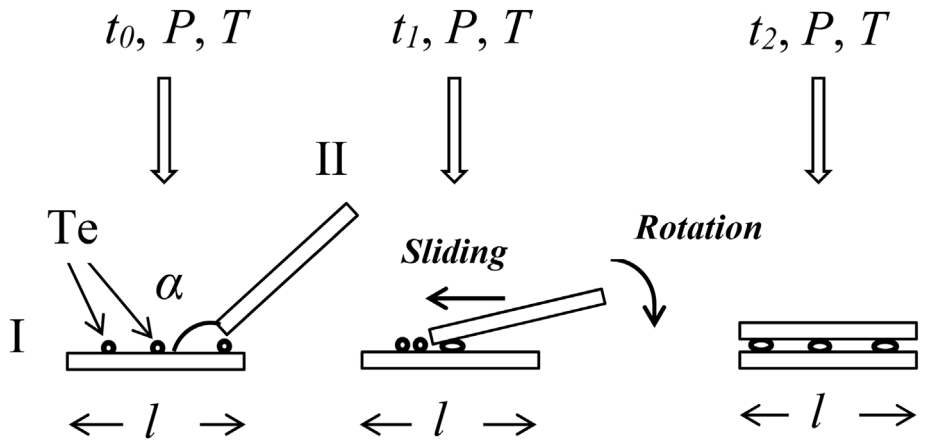

Fig. 4. Schematic of rearrangement of two plate-shaped particles under the packing of the starting powder under the SPS process.

attributed to forming the anti-site Bi_{Te} and R_{Te} defects, since the Bi or *R* atoms can easily jump from Bi site to Te site [46,47]. Owing to the high-temperature Te evaporation, the vacancies at Te sites, $V_{Te}^{\%\%}$, are formed. Each positively charged $V_{Te}^{\%\%}$ vacancy leaves two free electrons, which are majority carriers. The anti-site Bi_{Te} or R_{Te} defects contributes one hole as a free carrier and, hence, reduces a fraction of the electrons as majority carriers. The electronegativity values are equal to 2.10, 2.02 and 1.20 for Te, Bi and Gd, respectively. Therefore, larger difference in the electronegative for Gd-Te pair compared to the Bi-Te pair will decrease the concentration of the anti-site defects at Te-sites which contributes one hole per defect and, hence, will result in more electrons. For the Te-rich Bi_2Te_3 compounds, forming the anti-site Bi_{Te} or Gd_{Te} defects cannot be involved to explain the $n(x)$ dependence (Fig. 3 (a), since the Te content in these compounds is above the Te-stoichiometric value (Fig. 1 (a)), excluding the composition with 1 at. % Gd, which is very close to the Te-stoichiometric composition. In this case, the high-temperature Te evaporation cannot form the $V_{Te}^{\%\%}$ vacancies, which are needed to form the ant-site defects. Therefore, other point defects should be involved. Since the Te-rich $Bi_{2-x}Gd_xTe_{3+y}$ compounds are the nonstoichiometric compounds of cation interstitialcy type, the interstitial Te atoms will be intrinsic and typical defects for these compounds [41]. As was mentioned above, forming these defects can be responsible for gradual increasing in lattice *c* parameter with increasing *x* (Fig. 2 (b)). Besides, the anti-site Te_{Bi} defects can be also formed in the Te-rich compositions. Owing to difference in valence of the Te^{3+} and Bi^{2+} atoms, these point defects will behave as donor centres. As result, the electron concentration in the Te-rich $Bi_{2-x}Gd_xTe_{3+y}$ compounds will be gradually increasing with increasing excess Te content. This tendency was earlier reported and discussed in Ref. [48].

The bulk $Bi_{2-x}Gd_xTe_{3+y}$ compounds were found to be highly texturing during SPS-process. The texturing is specific feature of Bi_2Te_3-based alloys, which are sintering under uniaxial mechanical loading (SPS-pressing direction) and high-temperature treatment of a starting powder, consisting of 2D-particles [49–56]. In this case, texturing axis is oriented along the loading direction. Under the texturing, a lamellar grain texture is forming. The grains are elongated along the lamellar sheets, whereas the sheets lie in a plane, perpendicular to the texturing axis. SEM images of the grain structure taken on the fractured surfaces of the bulk $Bi_{2-x}Gd_xTe_{3+y}$ sample with x=0.2, which are oriented parallel and perpendicularly to the texturing axis, are shown in Fig. S2. Average grain sizes corresponding to directions, which are perpendicular ($d_\perp$) and parallel ($d_\parallel$) to the loading direction, were estimated. The $d_\perp$ and $d_\parallel$ sizes happened to be equal to ~800 nm and ~80 nm, respectively, and they were *x*-independent. That is, similarly to the 2D-particles in the starting $Bi_{2-x}Gd_xTe_{3+y}$ powders, the grains in the relevant bulk samples are also 2D-objects. The Lotgering factor, *LF*, was involved to characterize a texturing degree of all the samples. *LF*, calculated via analysis of XRD patterns taken for the $Bi_{2-x}Gd_xTe_{3+y}$ compounds with different *x*, is expressed as [57].

$$F = \frac{p - p_0}{1 - p_0} \tag{4}$$

where *p* and p_0 are given as

$$p = \frac{I(00l)}{\sum I(hkl)} \text{ and } p_0 = \frac{I_0(00l)}{\sum I_0(hkl)} \tag{5}$$

Here the *I* and I_0 intensities correspond to textured and non-textured samples, respectively. In limiting cases, $F \to 1$ is for ideally textured (single crystal) samples, and $F \to 0$ is for completely non-textured samples (powder or grained material with completely random grain orientation). To analyze the intensities in XRD pattern for the non-textured samples, XRD patterns taken for the starting powders were applied.

The $LF(x)$ dependence is presented in Fig. 3 (b). Above x>2 at. % Gd, *LF* is abruptly growing. Excess Te content in the bulk samples can be responsible for this $LF(x)$ feature. Under SPS-process, some fraction of excess Te can be released as Te inclusions at grain boundaries. Initial stage of SPS-process is packing of randomly oriented particles of a starting powder, occurring under constant external pressure, *P*, and constant temperature, *T* [58]. For the initial stage, a grain growth can be ignored. Then densification of the powder being sintered can be dominantly attributed to rotation and sliding of particles. During the texturing, the packing results in a rearrangement of particles into ordered lamellar sheets with preferential particles orientation. It is known that some nanometer powder can act as lubricants, improving the particles packing behavior during SPS-process. This lubricant effect was earlier reported for the Ce lubricant in Al_2O_3 [59] or the Te lubricant in Bi_2Te_3 [48]. Via the lubricating mechanism, increasing the Te content will result in more effective packing the particles that will result in relevant increasing preferential grain orientation. As result, the Lotgering factor is growing. The rotation and sliding processes for two plate-shaped particles with equal size *l*, denoted as I and II, are schematically demonstrated in Fig. 4. During a densification of the starting powder, the Te inclusions can act as lubricant between two contacting particles.

Single-crystalline Bi_2Te_3 and Bi_2Te_3-based compounds are high-anisotropic. This anisotropy is directly connected with their layered structure. The physical properties, measured along the layers or perpendicular to the layers, are remarkably different. Anisotropy in the specific electrical resistivity and the thermal conductivity is expressed by the ρ_c/ρ_{ab} and k_c/k_{ab} coefficients (here the *c* and *ab* subscripts correspond to the directions perpendicular or parallel to the layers, respectively). For single-crystalline Bi_2Te_3, these coefficients are $\rho_c/\rho_{ab} \sim 5 \div 5.5$ and $k_c/k_{ab} \sim 2$ [17]. Unlike *k* and ρ, the Seebeck coefficient is far less anisotropic quantity. Under texturing, preferential grain orientating in grained

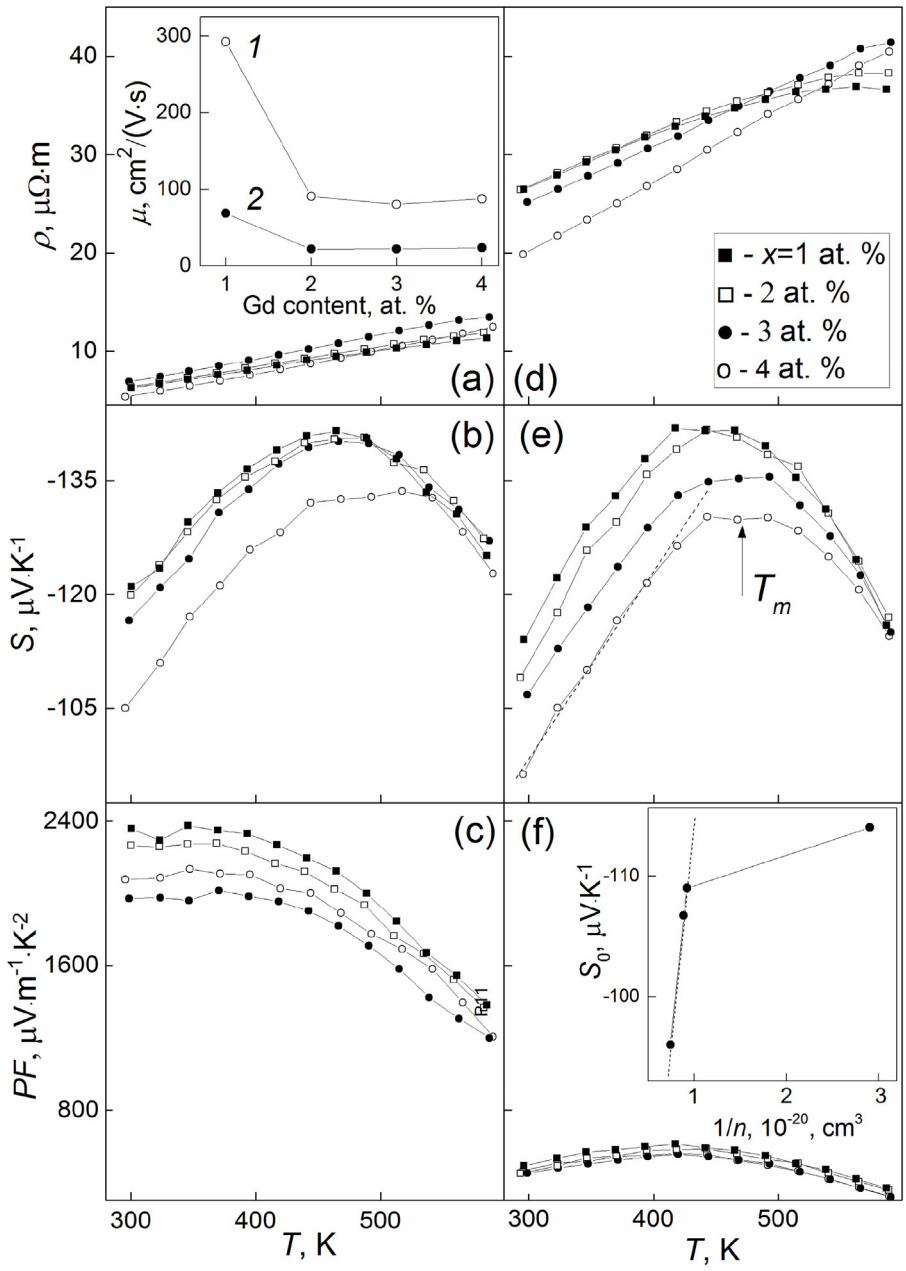

Fig. 5. Temperature dependences of ρ ((a) and (d)), S ((b) and (e)) and PF ((c) and (f)), taken for the $Bi_{2-x}Gd_xTe_{3+y}$ compounds at the perpendicular (left panel) and parallel (right panel) measuring orientations. Inset in Fig. (a) shows the Gd doping effect on the Hall electron mobilities, measured at the perpendicular (curve *1*) and parallel (*2*) measuring orientations. Inset to Fig. (f) shows the S_0 vs. $1/n$ dependence.

Bi_2Te_3 and Bi_2Te_3-based compounds will take place. This grain orienting can recover, at least, partially the anisotropy in the transport properties. Therefore, the transport properties of these grained materials, measured along the texturing direction (parallel measuring orientation) or within the plane perpendicular to this direction (perpendicular measuring orientation), start to be different again.

The $\rho(T)$ dependences taken for the $Bi_{2-x}Gd_xTe_{3+y}$ compounds at perpendicular and parallel measuring orientations are shown in Fig. 5 (a) and (d), respectively. The electrical resistivity for the perpendicular measuring orientation is much less as compared to that for the parallel orientation. This feature is natural, since for the perpendicular orientation is dominantly governed by the ρ_{ab} resistivity, whereas the ρ_c resistivity is dominantly contributing into ρ for the parallel orientation, and $\rho_{ab}<\rho_c$. Hence, the texturing just redistributes the ρ_c and ρ_{ab} contributions into the total resistivity that results in partial recovering in the ρ anisotropy. The Gd doping results in increasing in ρ. This Gd doping effect can be attributed to both the increasing n (Fig. 3 (a)) and the decreasing electron mobility. With increasing x, content of various point defects like the interstitial Te and anti-site Te_{Bi} defects should be increasing. These defects are scattering centres for electrons, affecting the mobility. The Gd doping effect on the Hall electron mobilities, measured at the perpendicular and parallel orientations, are shown in inset to Fig. 5 (a). The mobility for the perpendicular orientation is higher than for the parallel orientation. Both mobilities are highest for the composition with 1 at. % Gd. This composition is close to the Te-stoichiometric composition and it should content minimum quantity of point defects, related to destroying the Te-stoichiometry. The electron mobilities for the other compositions are very weakly x-dependent.

The resistivity of all the samples, measured at the perpendicular and parallel orientations, gradually increases with growing temperature

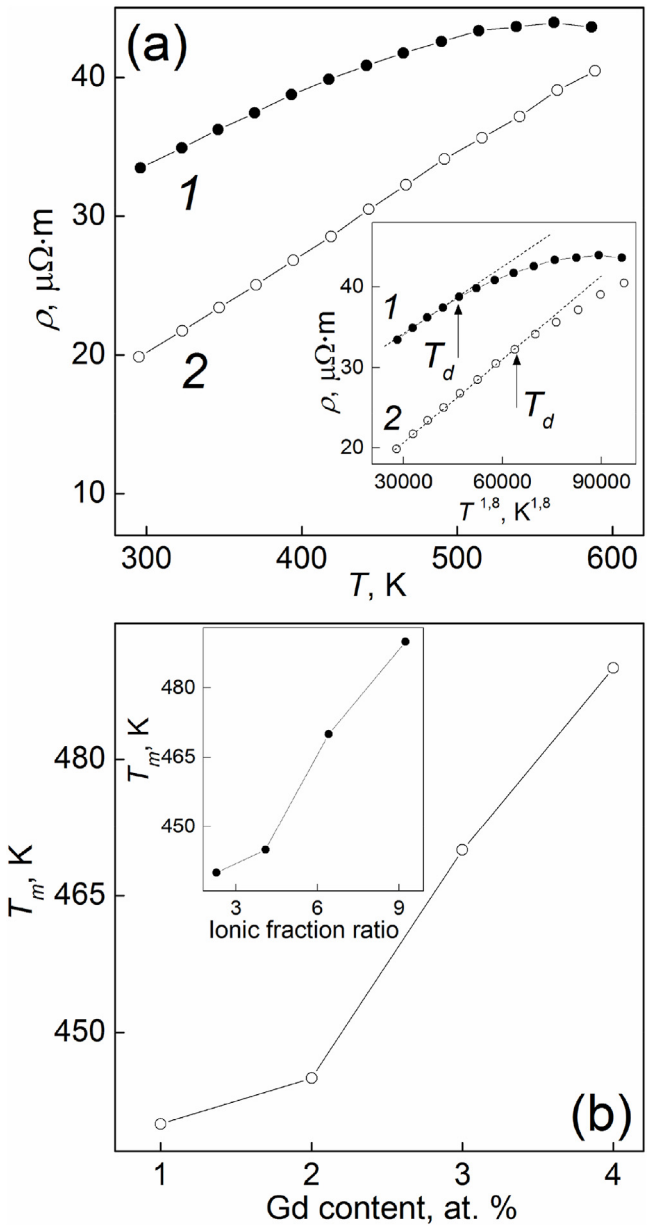

Fig. 6. (a) Temperature dependences of the specific electrical resistivity, measured at parallel orientation, for the $Bi_{2-x}Gd_xTe_{3+y}$ compounds with 1 (curve *1*) and 4 at. % Gd (*2*). Inset is the $\rho(T^{1.8})$ dependences for the same compounds; (b) Effect of Gd doping on the temperature position of the $S(T)$ maximum, measured at parallel orientation, for the $Bi_{2-x}Gd_xTe_{3+y}$ compounds. Inset is the T_m versus ionic fraction ratio dependence for the same compounds.

within whole temperature range from 290 K up to 600 K. This $\rho(T)$ behavior, which is characteristic for degenerate semiconductors and metals, is governed by temperature behavior of the electron mobility, whereas the electron concentration is T-independent. Depending on x, the $\rho(T)$ behavior is slightly changed. This change is illustrated by Fig. 6 (a), where the $\rho(T)$ curves are compared for the samples with 1 and 4 at. % Gd. These curves, measured for the parallel orientation, are crossing with each other at high temperatures. To show difference in the $\rho(T)$ behavior for these samples more clearly, the $\rho(T)$ curve for the sample with 1 at. % Gd, is shifted upwards by 7 μΩ m. For the sample with 4 at. % Gd, ρ is steady growing with increasing temperature. However, for the sample with 1 at. % Gd, ρ is gradually saturating at high temperatures with clear tendency to form the $\rho(T)$ maximum. Usually, for degenerate semiconductors the $\rho(T)$ dependence obeys the following expression

$$\rho(T) \sim T^{m} \tag{6}$$

where m is the constant.

The m is equal to 3/2 for, if acoustic phonon scattering of electrons takes place. This scattering is observed below the Debye temperature. Above room temperature, both acoustic and optical phonon scattering are dominant scattering mechanism for Bi_2Te_3-based compounds, resulting in $m>3/2$ [60]. For $Bi_{1.9}Gd_{0.1}Te_3$, m=1.8 was earlier reported [38]. Therefore, the $\rho(T)$ dependences in Fig. 6 (a) were also replotted as the $\rho(T^{1.8})$ dependences (inset to Fig. 6 (a)). The $\rho(T^{1.8})$ dependences are linear up to temperature T_d, above which a deviation from T-linear behavior is observed. The $\rho(T)$ deviation from regime of degenerate semiconductor is originated from onset of intrinsic electrical conductivity due to a thermal excitation of electrons from valence band to conduction band. The T_d temperature is shifting to high temperatures with increasing x. This tendency will be discussed below.

The $S(T)$ dependences for the $Bi_{2-x}Gd_xTe_{3+y}$ samples, measured at perpendicular and parallel orientations, are shown in Fig. 6 (b) and (e), respectively. The Seebeck coefficient is negative that corresponds to electron conductivity of the samples. The highest S is observed for the sample with 1 at.% Gd, whereas the sample with 4 at. % Gd is characterized by minimal S. All the $S(T)$ curves are bell-shaped. The S maxima are observed at temperature T^*. These maxima are originated from a bipolar effect, which is characteristic for Bi_2Te_3-based compounds [42–45]. Below T^*, the $S(T)$ dependences are close to linear ones, as is shown for the sample with 4 at. % Gd at the parallel measuring orientation. It is known [44] that the Seebeck coefficient of the degenerate semiconductors is expressed as

$$S = \frac{2k_B^2 T m^*}{3e\hbar^2}\left(\frac{\pi}{3n}\right)^{2/3}\left(\frac{3}{2}+\gamma\right) \tag{7}$$

where k_B is the Boltzmann's constant, $\hbar$ is the reduced Planck constant, m^* is the density-of-state effective mass of electrons and γ is the scattering factor.

Therefore, the low-temperature T-linear parts in the $S(T)$ dependences are in agreement with expression (7). Moreover, this expression also shows that the higher concentration of electrons will result in decreasing in S. The S_0 versus $1/n$ dependence is presented in inset to Fig. 4 (e) (here S_0 is the Seebeck coefficient, measured at room temperature at the parallel orientation). Excluding the sample with 1 at. % Gd, the $S_0(1/n)$ dependence is linear for other Te-rich samples (with very weakly x-dependent Hall mobility), obeying expression (7). The sample with 1 at. % Gd is close to the Te-stoichiometric composition. Therefore, for this sample a number of various defects, related to destroying the Te-stoichiometry, is minimal. As result, the scattering factor for the Te-rich and Te-stoichiometric compositions can be different. Similarly to the $T_d(x)$ behavior, observed in $\rho(T)$ measuring of the $Bi_{2-x}Gd_xTe_{3+y}$ compounds with different x (Fig. 5 (a)), the T_m temperature indicating the $S(T)$ maximum is also shifting to higher temperatures with increasing x.

The $T_m(x)$ dependence, which was extracted from the $S(T)$ dependences, measured at the parallel orientation, is shown in Fig. 6 (b). This dependence can be due to shifting in onset of the intrinsic electrical conductivity to high temperatures with increasing x. In turn, this shifting can be related to increasing in energy gap, E_g. As was discussed above, increasing x in $Bi_{2-x}Gd_xTe_{3+y}$ should result in relevant increasing the ionic bonding fraction (Fig. 2 (a)), and in relevant increasing the energy of polar covalent bond (expression (3)). In turn, E_g for many covalent-ionic semiconductor increases with increasing this energy in accordance with empirical Manka expression [61].

$$E_g = a(E_S - b) \tag{8}$$

where E_S is the single bond energy, and a and b are the constants.

Expression (8) was successfully applied to analyze the Eg versus E_S dependence for 52 binar semiconductors [62]. For these semiconductors,

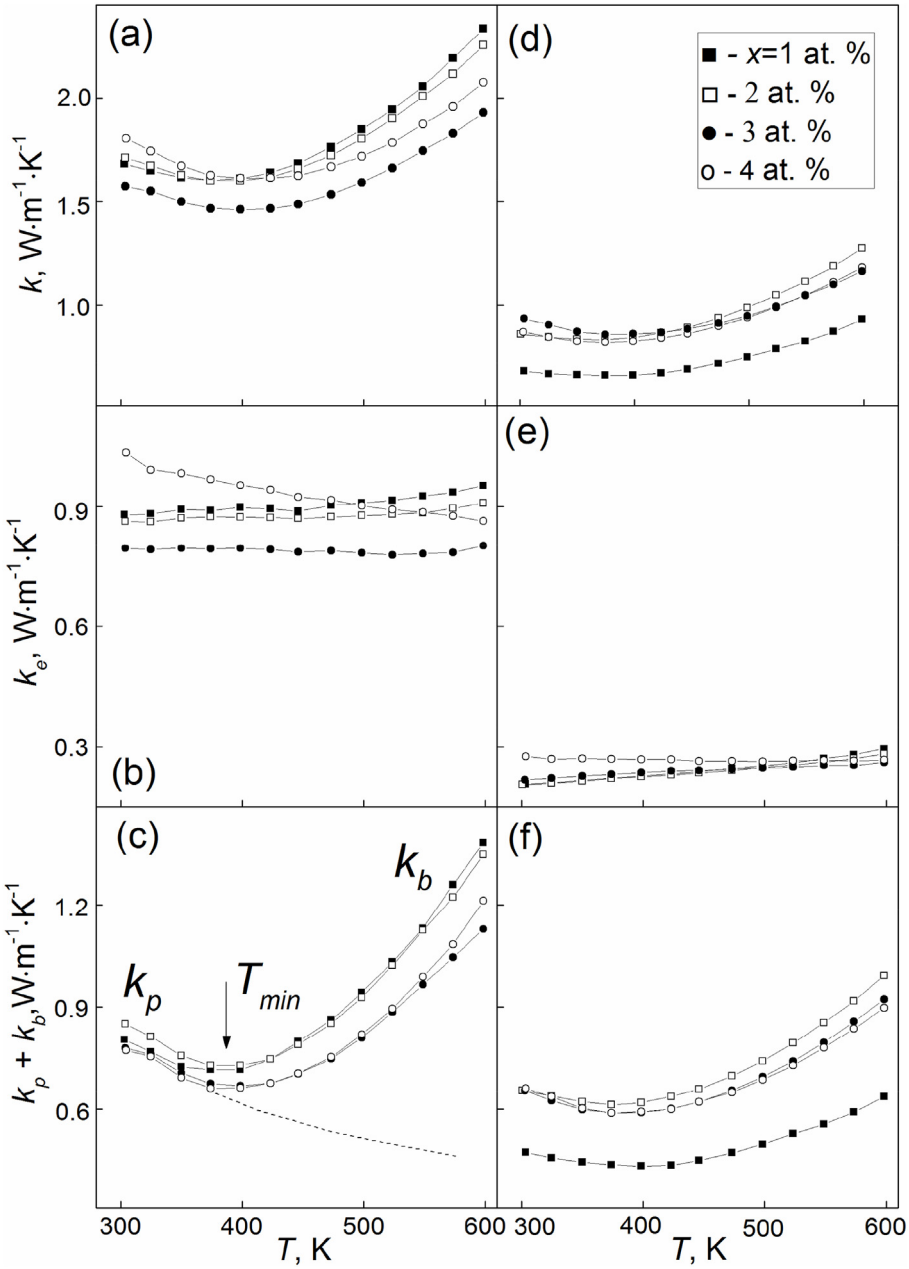

Fig. 7. Temperature dependences of k ((a) and (d)), k_e ((b) and (e)) and $k_p + k_b$ ((c) and (f)), taken for the $Bi_{2-x}Gd_xTe_{3+y}$ compounds at the perpendicular (left panel) and parallel (right panel) measuring orientations.

their energy gap was found to be progressively increasing with increasing E_S. This tendency is a result of increasing the ionicity bonding degree in chemical bonds of these compounds. The T_m versus ionic fraction ratio dependence for the $Bi_{2-x}Gd_xTe_{3+y}$ compounds is plotted in inset to Fig. 6 (b). Under the intrinsic electrical conductivity, the thermal excitation of electrons from valence band to conduction band is governed by a thermal energy of electrons, which is proportional to k_BT. Therefore, the shifting T_m to high temperatures with increasing x (or with increasing the ionicity bonding degree) can be attributed to increasing in the energy gap, which electrons should be overcome via the thermal generation.

The temperature dependences of the power factor, *PF*, calculated as $PF=S^2/\rho$ for the perpendicular and parallel measuring orientations, are shown in Fig. 5 (c) and (f), respectively. Since ρ for the perpendicular orientation is much lower than ρ for the parallel orientation and S for both measuring orientations are close to each other, *PF* for the perpendicular orientation is much more than *PF* for the parallel orientation. The highest *PF* value for both measuring orientations is observed for the $Bi_{2-x}Gd_xTe_{3+y}$ samples with different x.

The temperature dependences of the total thermal conductivity and different contributions into the total thermal conductivity, taken at the perpendicular and parallel measuring orientations, are shown in Fig. 7. The total thermal conductivity of all the samples, measured at the perpendicular orientation, is higher as compared to that for the parallel orientation. This behavior is expected, since for the perpendicular orientation, k is dominantly governed by the k_{ab} component, whereas the k_c component is dominantly contributing into k for the parallel orientation, and $k_{ab} > k_c$. Similarly to features in the specific electrical resistivity of the textured $Bi_{2-x}Gd_xTe_{3+y}$ samples (Fig. 5 (a) and (d)), the texturing results in partial recovering in the k anisotropy via redistributing of the k_c and k_{ab} contributions into the total thermal conductivity. In general, the total thermal conductivity of semiconductor is combined from the lattice (or phonon) thermal conductivity, k_p, the electronic thermal

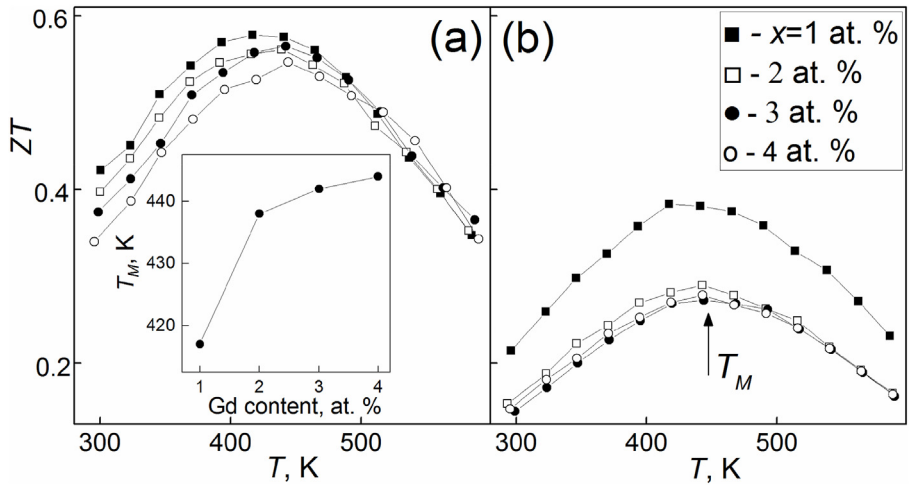

Fig. 8. Temperature dependences of the thermoelectric figure-of-merit, taken for the $Bi_{2-x}Gd_xTe_{3+y}$ compounds at the perpendicular (a) and parallel (b) measuring orientations. Inset is the T_M versus Gd content dependence.

conductivity, k_e, and the bipolar thermal conductivity, k_b. To find k_e, the Wiedemann-Franz law is usually applied, which is given by expression [63].

$$k_e = \frac{LT}{\rho} \tag{9}$$

where L is the Lorenz number.

To correctly estimate the Lorenz number, approach proposed in Ref. [64] was applied. In accordance with this approach, the Lorenz number and maximum value of the Seebeck coefficient, S_{max}, are connected to each other by expression

$$L\left[10^{-8},\ \mathrm{W\%\Omega\%K^{-2}}\right] = 1.5 + \exp\left(-\frac{|S|_{max}[\mu\mathrm{V\%K^{-1}}]}{116}\right) \tag{10}$$

For all the $Bi_{2-x}Gd_xTe_{3+y}$ samples, L was estimated as $\sim 1.8 \times 10^{-8}$ $\mathrm{W\Omega \cdot K^{-2}}$. Next, using Wiedemann-Franz law, the $k_e(T)$ contributions for the perpendicular and parallel measuring orientations were extracted (Fig. 7 (b) and (e)). These contributions are governed by the $\rho(T)$ behavior. Owing to lower ρ, the k_e contribution for the perpendicular orientation is much more as compared to that for the parallel orientation. Using the $k_e(T)$ contributions, sums of the lattice and bipolar thermal conductivity contributions for the perpendicular and parallel measuring orientations were found as $k_p(T)+k_b(T)=k(T)-k_e(T)$ (Fig. 7 (c) and (f)). All the $k_p(T)+k_b(T)$ curves have minima at temperature T_{min}. This temperature is indicated by arrow for the composition with 4 at. % Gd in Fig. 7 (c). The $T_{min}(x)$ dependence is in well agreement with the $T_m(x)$ dependence (Fig. 5 (b)). In this case, the T_{min} temperature separates different mechanisms of the thermal conductivity. Below T_{min}, the $k_p(T)+k_b(T)$ contributions are gradually decreasing with increasing temperature. This behavior is characteristic for the lattice thermal conductivity, which is varied as T^{-1} above the Debye temperature [63]. In fact, the $k_p(T)$ dependences obey the $k_p \sim T^{-1}$ law for temperatures below minima in the $k_p(T)+k_b(T)$ curves, as is shown by dashed line for the composition with 4 at. % Gd in Fig. 6 (c). Above T_{min}, the $k_p(T)+k_b(T)$ contributions are already growing with increasing temperature that is originated from the bipolar thermal conductivity [65]. At the bipolar thermal conductivity, electron-hole pairs, thermally excited at hot-side of sample via the intrinsic conductivity, transfer to cold-side to disappear due to a recombination process, which is accompanied by emerging phonon. The energy of recombination per one electron-hole pair will be equal or greater than energy gap.

No clear correlation between the k, k_e k_p+k_b contributions and x can be found for the perpendicular and parallel measuring orientations. However, one can note that among all the samples studied, the k_p contribution is least for the composition with 1 at. % Gd for the parallel measuring orientation. This composition is very close to the Te-stoichiometric one. As was mentioned above, excess Te can be released as Te inclusions at grain boundaries, acting as a lubricant during densification of the starting powders. These inclusions, owing to high thermal conductivity of Te (~2 W m^{-1} K^{-1} [66]), could enhance the thermal conductivity of the $Bi_{2-x}Gd_xTe_{3+y}$ compounds for parallel measuring orientation. Since the Te inclusions cannot be formed in the composition with 1 at. % Gd, this composition should have the minimal k_p contribution.

The $\rho(T)$, $S(T)$ and $k(T)$ dependences are well reproducible for several consecutive heating cycles of the samples being studied. Therefore, one can conclude no change in elemental composition of the samples, affecting their thermoelectric properties, takes place during measurement of the properties.

Finally, the $\rho(T)$, $S(T)$ and $k(T)$ contributions, measured for both orientations, were used to calculate the thermoelectric figure of merit $ZT=(TS^2)/(\rho k)$ for the samples with different x (Fig. 7). The ZT for the perpendicular orientation is much more than for the parallel orientation. For the perpendicular orientation, low ρ, which is favoring to enhancing ZT, but high k, which is harmful for enhancing ZT, are simultaneously combined. Since the ρ contribution is dominant, ZT is enhancing. All the curves in Fig. 8 are bell-like shaped with maxima at temperatures T_M, which is x-dependent and falling in the 415–450 K interval (inset to Fig. 8). This T_M shifting is due to similar x-effect on the $\rho(T)$, $S(T)$ and $k(T)$ dependences. The highest ZT is observed for the composition with 1 at. % Gd. These values are equal to ~0.57 and ~0.38 for the perpendicular and parallel measuring orientations, respectively. These values are in agreement with data, reported for Bi_2Te_3, doped by rare earth elements and prepared by solvothermal synthesize and spark plasma sintering [43,45,67,68].

4. Conclusion

Thus, under the gradual Gd doping of Bi_2Te_3, the Te content is simultaneously changing. Changing the Te-stoichiometry is due to the high-temperature Te evaporation during spark plasma sintering. Owing to difference in electronegativity of Bi and Gd, the ionicity degree and the strength of polar covalent Bi(Gd)-Te bonds are increasing with increasing the Gd content. As result, the rate of the Te evaporation decreases. So, the x and y coefficients the $Bi_{2-x}Gd_xTe_{3+y}$ compounds are interconnected. Changes in crystal lattice parameters, concentration and mobility of electrons of the Te-rich $Bi_{2-x}Gd_xTe_{3+y}$ compounds can be due the interstitial Te atoms and anti-site Te_{Bi} defects, formed via direct Gd doping,

which is accompanied by indirect Te-stoichiometry destroying. The electron concentration affects the specific electrical resistivity, the Seebeck coefficient and the electronic contribution into the total thermal conductivity. Optimal electron concentration corresponds to the almost Te-stoichiometric composition with 1 at. % Gd and 59.94 at. % Te.

In the papers [38,56], effects of high-temperature treatment on elemental composition, crystal and grain structures and thermoelectric properties of non-textured [38] and textured [56] $Bi_{1.9}Gd_{0.1}Te_3$ samples have been reported. However, only composition with 2 at. % Gd was studied. Besides, the starting powders, applied to prepare the bulk samples, were Te-stoichiometric. Changes in the grain structure (grain size, texturing degree) in the samples were induced by changing in temperature of the high-temperature treatment. These changes were dominantly analysed. Under the high-temperature treatment, the Te evaporation also occurred. The rate of the evaporation was strongly and naturally dependent on temperature of the high-temperature treatment. Namely, increasing in this temperature resulted in decreasing the Te content in the $Bi_{1.9}Gd_{0.1}Te_3$ samples. The novel finding of present work is finding and examining the Te-stoichiometry destroying in Bi_2Te_3 under the Gd doping. Moreover, a degree of this destroying is governed by the Gd content, provided that the technological parameters for preparing samples with different Gd content are the same. Therefore, elemental doping of Bi_2Te_3-based compounds can result in the Te-stoichiometry destroying in uncontrolled manner that will additionally affect the thermoelectric properties of the compounds.

CRediT authorship contribution statement

Maxim Yaprintsev: Investigation. **Oleg Ivanov:** Writing – review & editing. **Alexei Vasil'ev:** Investigation.

Declaration of competing interest

The authors declare that they have no known competing financial interests or personal relationships that could have appeared to influence the work reported in this paper.

Acknowledgements

This work was supported by the Ministry of Science and Higher Education of Russian Federation (grant number No 0625-2020-0015). All of studies were carried out by the scientific equipment of joint research center “Technologies and Materials” at the Belgorod State University.

Appendix A. Supplementary data

Supplementary data to this article can be found online at https://doi.org/10.1016/j.jssc.2022.122945.

References

[1] H. Scherrer, S. Scherrer, Thermoelectrics Handbook: Macro to Nano, CRC Taylor and Francis, Boca Raton, 2012.
[2] G.S. Nolas, J. Sharp, H.J. Goldsmid, Thermoelectrics Basic Principles and New Materials Developments, Springer, Berlin, 2001.
[3] T. Moria, A. Maignan, Thermoelectric materials developments: past, present, and future, Sci. Technol. Adv. Mater. 22 (2021) 998–999, https://doi.org/10.1080/14686996.2021.1966242.
[4] H. Nakatsugawa, T. Ozaki, H. Kishimura, Y. Okamoto, Thermoelectric properties of Heusler Fe_2TiSn alloys, J. Electron. Mater. 49 (2019) 1051–1060, https://doi.org/10.1007/s11664-019-07855-7.
[5] A. Nozariasbmarz, A. Agarwal, Z.A. Coutant, M.J. Hall, J. Liu, R. Liu, A. Malhotra, P. Norouzzadeh, M.C. Öztürk, V.P. Rames, Y. Sargolzaeiaval, F. Suarez, D. Vashaee, Thermoelectric silicides: a review, Japan, J. Appl. Phys. 56 (2017) 1–27, https://doi.org/10.1016/j.jallcom.2016.07.187, 05DA04.
[6] S. Li, X. Lou, X. Li, J. Zhang, D. Li, H. Deng, J. Liu, G. Tang, Realization of high thermoelectric performance in polycrystalline tin selenide through Schottky vacancies and endotaxial nanostructuring, Chem. Mater. 32 (2020) 9761–9770, https://doi.org/10.1021/acs.chemmater.0c03657.
[7] A.V. Powell, 2.6 - high-performance sulfide thermoelectric materials, Editor(s): ryoji Funahashi, in: Woodhead Publishing Series in Electronic and Optical Materials, Thermoelectric Energy Conversion, Woodhead Publishing, 2021.
[8] O. Ivanov, M. Yaprintsev, A. Vasil'ev, E. Yaprintseva, Microstructure and thermoelectric properties of the medium-entropy block-textured $BiSbTe_{1.5}Se_{1.5}$ alloy, J. Alloys Compd. 872 (2021) 1–7, https://doi.org/10.1016/j.jallcom.2021.159743, 159743.
[9] Z. Fan, H. Wang, Y. Wu, X.J. Liu, Z.P. Lu, Thermoelectric high-entropy alloys with low lattice thermal conductivity, RSC Adv. 6 (2016) 52164–52170, https://doi.org/10.1039/c5ra28088e.
[10] K. Koumoto, I. Terasaki, R. Funahashi, R. Funahashi, Complex oxide materials for potential thermoelectric applications, MRS Bull. 31 (2006) 206–210, https://doi.org/10.1557/mrs2006.46.
[11] W. Saito, K. Hayashi, J. Dong, J.F. Lee, Y. Miyazaki, Control of the thermoelectric properties of Mg_2Sn single crystals via point-defect engineering, Sci. Rep. 10 (2020) 1–8, https://doi.org/10.1038/s41598-020-58998-1, 2020.
[12] X. Dong, W. Cui, W.-D. Liu, S. Zheng, L. Gao, L. Yue, Y. Wue, B. Wang, Z. Zhang, L. Chen, Z.-G. Chen, Synergistic band convergence and defect engineering boost thermoelectric performance of SnTe, J. Mater. Sci. Technol. 86 (2021) 204–209, https://doi.org/10.1016/j.jmst.2021.01.040.
[13] C. Zhou, Y.K. Lee, J. Cha, B. Yoo, S.P. Cho, T. Hyeon, I. Chung, Defect engineering for high-performance n-type PbSe thermoelectrics, J. Am. Chem. Soc. 140 (2018) 9282–9290, https://doi.org/10.1021/jacs.8b05741.
[14] M.G. Kanatzidis, Nanostructured thermoelectrics: the new paradigm? Chem. Mater. 22 (2010) 648–659, https://doi.org/10.1021/cm902195j.
[15] A.J. Minnich, M.S. Dresselhaus, Z.F. Ren, G. Chen, Bulk nanostructured thermoelectric materials: current research and future prospects, Energy Environ. Sci. 2 (2009) 466–479, https://doi.org/10.1039/B822664B.
[16] R. Mohanraman, T.-W. Lan, T.-C. Hsiung, D. Amada, P.-C. Lee, M.-N. Ou, Y.-Y. Chen, Engineering nanostructural routes for enhancing thermoelectric performance: bulk to nanoscale, Front. Chem. 10 (2015) 1–9, https://doi.org/10.3389/fchem.2015.00063.
[17] H.J. Goldsmid, Bismuth telluride and its alloys as materials for thermoelectric generation, Materials 7 (2014) 2577–2592, https://doi.org/10.3390/ma7042577.
[18] Y. Pan, T.R. Wei, C.F. Wu, J.F. Li, Electrical and thermal transport properties of spark plasma sintered *n*-type $Bi_2Te_{3-x}Se_x$ alloys: the combined effect of point defect and Se content, J. Mater. Chem. C. 3 (2015) 10583–10589, https://doi.org/10.1039/C5TC02219C.
[19] L. Hu, T. Zhu, X. Liu, X. Zhao, Point defect engineering of high-performance bismuth-telluride-based thermoelectric materials, Adv. Funct. Mater. 24 (2014) 5211–5218, https://doi.org/10.1002/adfm.201400474.
[20] J. Suh, K.M. Yu, D. Fu, X. Liu, F. Yang, J. Fan, D.J. Smith, Y.H. Zhang, J.K. Furdyna, C. Dames, W. Walukiewicz, J. Wu, Simultaneous enhancement of electrical conductivity and thermopower of Bi_2Te_3 by multifunctionality of native defects, Adv. Mater. 27 (2015) 3681–3686, https://doi.org/10.1002/adma.201501350.
[21] Y. Liu, M. Zhou, J. He, Towards higher thermoelectric performance of Bi_2Te_3 via defect engineering, Scr. Mater. 111 (2015) 39–73, https://doi.org/10.1016/j.scriptamat.2015.06.031.
[22] H. Zhu, J.-Y. Zhao, C. Xiao, Improved thermoelectric performance in *n*-type BiTe facilitated by defect engineering, Rare Met. 40 (2021) 2829–2837, https://doi.org/10.1007/s12598-021-01737-w.
[23] M. Hong, Z.-G. Chen, J. Zou, Fundamental and progress of Bi_2Te_3-based thermoelectric materials, Chin. Phys. B 27 (2018) 1–46, https://doi.org/10.1088/1674-1056/27/4/048403, 048403.
[24] L. Hu, T. Zhu, X. Liu, X. Zhao, Point defect engineering of high-performance bismuth-telluride-based thermoelectric materials, Adv. Funct. Mater. 24 (2014) 5211–5218, https://doi.org/10.1002/adfm.201400474.
[25] O. Ivanov, M. Yaprintsev, R. Lyubushkin, O. Soklakova, Enhancement of thermoelectric efficiency in Bi_2Te_3 via rare earth element doping, Scr. Mater. 146 (2018) 91–94, https://doi.org/10.1016/j.scriptamat.2017.11.031.
[26] F. Wu, H. Song, J. Jia, X. Hu, Effects of Ce, Y, and Sm doping on the thermoelectric properties of Bi_2Te_3 alloy, Prog. Nat. Sci. Mater. Int. 23 (2013) 408–412, https://doi.org/10.1016/j.pnsc.2013.06.007.
[27] D. Souchay, M. Nentwig, D. Gunther, S. Keilholz, J. de Boor, A. Zeugner, A. Isaeva, M. Ruck, A.U.B. Wolter, B. Buchnerde, O. Oeckler, Layered manganese bismuth tellurides with $GeBi_4Te_7$- and $GeBi_6Te_{10}$-type structures: towards multifunctional materials, J. Mater. Chem. C. 7 (2019) 9939–9953, https://doi.org/10.1039/c9tc00979e.
[28] M. Nentwig, L. Eisenburger, F. Heinke, D. Souchay, O. Oeckler, A layered tin bismuth selenide with three different building blocks that account for an extremely large lattice parameter of 283 Å, Chem. Eur J. 26 (2020) 10676–10681, https://doi.org/10.1002/chem.202000663.
[29] W. Ma, M.-C. Record, J. Tian, P. Boulet, Strain effects on the electronic and thermoelectric properties of *n*(PbTe)-*m*(Bi_2Te_3) system compounds, Materials 14 (2021) 1–17, https://doi.org/10.3390/ma14154086, 4086.
[30] T.C. Harman, P.J. Taylor, M.P. Walsh, B.E. LaForge, Quantum dot superlattice thermoelectric materials and devices, Science 27 (2002) 2229–2232, https://doi.org/10.1126/science.1072886.
[31] J.-H. Bahk, Z. Bian, A. Shakouri, Electron transport modeling and energy filtering for efficient thermoelectric $Mg_2Si_{1-x}Sn_x$ solid solutions, Phys. Rev. B 89 (2017) 1–13, https://doi.org/10.1103/PhysRevB.89.075204, 075204.
[32] J.R. Drabble, C.H.L. Goodman, Chemical bonding in bismuth telluride, J. Phys. Chem. Solid. 5 (1958) 142–144, https://doi.org/10.1016/0022-3697(58)90139-2.
[33] S. Nakajima, The crystal structure of $Bi_2Te_{3-x}Se_x$, J. Phys. Chem. Solid. 24 (1963) 479–485, https://doi.org/10.1016/0022-3697(63)90207-5.
[34] L. Pauling, The Nature of the Chemical Bond', Oxford & IBH Pub. Co., Delhi, 1969.

[35] R.T. Sanderson, Electronegativity and bond energy, J. Am. Chem. Soc. 105 (1983) 2259–2261, https://doi.org/10.1021/ja00346a026.
[36] B.D. Cullity, C.D. Graham, Introduction to Magnetic Materials, IEEE Press, Piscataway, 2009.
[37] H. Osterhage, J. Gooth, B. Hamdou, P. Gwozdz, R. Zierold, K. Nielsch, Thermoelectric properties of topological insulator Bi2Te3, Sb2Te3, and Bi2Se3 thin film quantum wells, Appl. Phys. Lett. 105 (2014) 1–4, https://doi.org/10.1063/1.4896680, 123117.
[38] M. Yaprintsev, A. Vasiliev, O. Ivanov, Sintering temperature effect on thermoelectric properties and microstructure of the grained $Bi_{1.9}Gd_{0.1}Te_3$ compound, J. Eur. Ceram. Soc. 39 (2019) 1193–1205, https://doi.org/10.1016/j.jeurceramsoc.2018.12.041.
[39] R.D. Shannon, Revised effective ionic radii and systematic studies of interatomic distances in halides and chaleogenides, Acta Crystallogr. A32 (1976) 751–767. https://doi:10.1107/S0567739476001551.
[40] M. El Kholdi, M. Averous, S. Charar, C. Fau, G. Brun, H. Ghoumari-Bouanani, J. Deportes, Magnetic properties of a layered and anisotropic rhombohedral compound: $Bi_{2(1-x)}$ $Gd_{2x}Te_3$, Phys. Rev. B 49 (1994) 1711–1715, https://doi.org/10.1103/physrevb.49.1711.
[41] T. Zhu, L. Hu, X. Zhao, J. He, New insights into intrinsic point defects in V_2VI_3 thermoelectric materials, Adv. Sci. 3 (2016) 1–16, https://doi.org/10.1002/advs.201600004, 1600004.
[42] M. Yaprintsev, R. Lyubushkin, O. Soklakova, O. Ivanov, Effects of Lu and Tm doping on thermoelectric properties of Bi_2Te_3, J. Electron. Mater. 47 (2018) 1362–1370, https://doi.org/10.1007/s11664-017-5940-8.
[43] O. Ivanov, M. Yaprintsev, Mechanisms of thermoelectric efficiency enhancement in Lu-doped Bi_2Te_3, Mater. Res. Express 5 (2018) 1–10, https://doi.org/10.1088/2053-1591/aaa265, 015905.
[44] J. Yang, F. Wu, Z. Zhu, L. Yao, H. Song, X. Hu, Thermoelectrical properties of lutetium-doped Bi_2Te_3 bulk samples prepared from flower-like nanopowders, J. Alloys Compd. 619 (2015) 401–405, https://doi.org/10.1016/j.jallcom.2014.09.024.
[45] X.H. Ji, X.B. Zhao, Y.H. Zhang, B.H. Lu, H. Ni, Synthesis and properties of rare earth containing Bi_2Te_3 based thermoelectric alloys, J. Alloys Compd. 387 (2005) 282–286, https://doi.org/10.1016/j.jallcom.2004.06.047.
[46] J. Lee, A. Berger, L.U. Cagnon, U. Gosele, K. Nielsch, J. Lee, Disproportionation of thermoelectric bismuth telluride nanowires as a result of the annealing process, Phys. Chem. Chem. Phys. 12 (2010) 15247–15250, https://doi.org/10.1039/c0cp00749h.
[47] P. Lost'ák, C. Drasar, D. Bachan, L. Benes, A. Krejcová, Defects in $Bi_2Te_{3-x}Se_x$ single crystals, Radiat. Eff. Defect Solid 165 (2010) 211–215, https://doi.org/10.1080/10420151003616663.
[48] Y. Liu, Y. Zhang, K.H. Lim, M. Ibáñez, S. Ortega, M. Li, J. David, S. Martí-Sánchez, K.M. Ng, J. Arbiol, M.V. Kovalenko, D. Cadavid, A. Cabot, High thermoelectric performance in crystallographically textured *n*-type $Bi_2Te_{3-x}Se_x$ produced from asymmetric colloidal nanocrystals, ACS Nano 12 (2018) 7174–7184, https://doi.org/10.1021/acsnano.8b03099.
[49] M. Yaprintsev, A. Vasil'ev, O. Ivanov, Thermoelectric properties of the textured $Bi_{1.9}Gd_{0.1}Te_3$ compounds spark-plasma-sintered at various temperatures, J. Eur. Ceram. Soc. 40 (2020) 742–750. https://doi:10.1016/j.jeurceramsoc.2018.12.041.
[50] S.D. Bhame, D. Pravarthana, W. Prellier, J.G. Noudem, Enhanced thermoelectric performance in spark plasma textured bulk *n*-type $Bi_2Te_{2.7}Se_{0.3}$ and *p*-type $Bi_{0.5}Sb_{1.5}Te_3$, Appl. Phys. Lett. 102 (2013), https://doi.org/10.1063/1.4807771, 2190:1 - 3.
[51] X.A. Fan, J.Y. Yang, R.G. Chen, H.S. Yun, W. Zhu, S.Q. Bao, X.K. Duan, Characterization and thermoelectric properties of *p*-type 25%Bi_2Te_3–75%Sb_2Te_3 prepared via mechanical alloying and plasma activated sintering, J. Phys. D Appl. Phys. 39 (2006) 740–745, https://doi.org/10.1088/0022-3727/39/4/021.
[52] J. Jiang, L. Chen, S. Bai, Q. Yao, Q. Wang, Fabrication and thermoelectric performance of textured *n*-type $Bi_2(Te,Se)_3$ by spark plasma sintering, Mater. Sci. Eng. B 117 (2005) 334–338, https://doi.org/10.1016/j.mseb.2005.01.002.
[53] Q. Lognon, F. Gascoin, O.I. Lebedev, L. Lutterotti, S. Gascoin, D. Chateigner, Quantitative texture analysis of spark plasma textured *n*-Bi_2Te_3, J. Am. Ceram. Soc. 97 (2014) 2038–2045, https://doi.org/10.1111/jace.12970/.
[54] A. Vasil'ev, M. Yaprintsev, O. Ivanov, E. Danshina, Anisotropic thermoelectric properties of $Bi_{1.9}Lu_{0.1}Te_{2.7}Se_{0.3}$ textured via spark plasma sintering, Solid State Sci. 84 (2018) 28–430, https://doi.org/10.1016/j.solidstatesciences.2018.08.004.
[55] S. Miura, Y. Satob, K. Fukuda, K. Nishimura, K. Ikeda, Texture and thermoelectric properties of hot-extruded Bi_2Te_3 compound, Mater. Sci. Eng. A 277 (2000) 244–249, https://doi.org/10.1016/S0921-5093(99)00539-0.
[56] O. Ivanov, M. Yaprintsev, A. Vasil'ev, Comparative analysis of the thermoelectric properties of the non-textured and textured $Bi_{1.9}Gd_{0.1}Te_3$ compounds, J. Solid State Chem. 290 (2020) 1–10, https://doi.org/10.1016/j.jssc.2020.121559, 121559.
[57] F.K. Lotgering, Topotactical reactions with ferrimagnetic oxides having hexagonal crystal structures—I, J. Inorg. Nucl. Chem. 9 (1959) 113–123, https://doi.org/10.1016/0022-1902(59)80070-1.
[58] L. Wang, V. Pouchly, K. Maca, Z. Shen, Y. Xiong, Intensive particle rearrangement in the early stage of spark plasma sintering process, J. Asian Ceram. Soc. 3 (2015) 183–187, https://doi.org/10.1016/j.jascer.2015.02.004.
[59] I. Alvarez-Clemares, G. Mata-Osoro, A. Fernandez, S. Lopez-Esteban, C. Pecharroman, J. Palomares, R. Torrecillas, J.S. Moya, Transparent alumina/ceria nanocomposites by spark plasma sintering, Adv. Eng. Mater. 12 (2010) 1154–1160, https://doi.org/10.1002/adem.201000176.
[60] D.A. Neamen, Semiconductor Physics and Devices, McGraw-Hill, New York, 2012.
[61] P. Manka, A relation between the binding energy and the band-gap energy in semiconductors of diamond or zinc-blende structure, J. Phys. Chem. Solid. 20 (1961) 268–273, https://doi.org/10.1016/0022-3697(61)90013-0.
[62] A.K. Vijh, Correlation between bond energies and forbidden gaps of inorganic binary compounds, J. Phys. Chem. Solid. 30 (1969) 1999–2005, https://doi.org/10.1016/0022-3697(69)90178-4.
[63] J.S. Blakemore, Solid State Physics, Cambridge University Press, Cambridge, 1985.
[64] H. Kim, Z. Gibbs, Y. Tang, H. Wang, G. Snyder, Characterization of Lorenz number with Seebeck coefficient measurement, Apl. Mater. 3 (2015) 1–5, https://doi.org/10.1063/1.4908244, 041506.
[65] S. Wang, J. Yang, T. Toll, J. Yang, W. Zhang, X. Tang, Conductivity-limiting bipolar thermal conductivity in semiconductors, Sci. Rep. 5 (2015) 1–5, https://doi.org/10.1038/srep10136, 10136.
[66] S. Sampath, K.V. Ramanaiah, Electrical, electromechanical and thermal properties of thin tellurium films, Bull. Mater. Sci. 7 (1985) 63–69, https://doi.org/10.1007/BF02744260.
[67] X.H. Ji, X.B. Zhao, Y.H. Zhang, B.H. Lu, H.L. Ni, Solvothermal synthesis and thermoelectric properties of lanthanum contained Bi–Te and Bi–Se–Te alloys, Mater. Lett. 59 (2005) 682–685, https://doi.org/10.1016/j.matlet.2004.11.008.
[68] F. Wu, H.Z. Song, J.F. Jia, F. Gao, Y.J. Zhang, X. Hu, Thermoelectric properties of Ce-doped n-type $Ce_xBi_{2-x}Te_{2.7}Se_{0.3}$ nanocomposites, Phys. Status Solidi 210 (2013) 1183–1189, https://doi.org/10.1002/pssa.201228589.